THE ASTROPHYSICAL JOURNAL, 496:490–502, 1998 March 20

THE COSMIC-RAY ^{3}He/^{4}He RATIO FROM 200 MeV PER NUCLEON^{-1} TO 3.7 GeV PER NUCLEON^{-1}

O. REIMER,[1] W. MENN, M. HOF, AND M. SIMON
Universität Siegen, D-57068 Siegen, Germany
A. J. DAVIS, A. W. LABRADOR, R. A. MEWALDT, AND S. M. SCHINDLER
California Institute of Technology, Pasadena, CA 91125
L. M. BARBIER, E. R. CHRISTIAN, K. E. KROMBEL, J. W. MITCHELL, J. F. ORMES, AND R. E. STREITMATTER
NASA Goddard Space Flight Center, Greenbelt, MD 20771
R. L. GOLDEN,[2] S. J. STOCHAJ, AND W. R. WEBBER
New Mexico State University, Las Cruces, NM 88003
AND
I. L. RASMUSSEN
Danish Space Research Institute, DK-2100 Copenhagen, Denmark
Received 1997 May 19; accepted 1997 October 24

ABSTRACT

The abundances of cosmic-ray helium isotopes between 0.2 and 3.7 GeV nucleon^{-1} were measured by the Isotope Matter Antimatter Experiment (IMAX) during a flight from Lynn Lake, Manitoba, Canada on 1992 July 16–17. The IMAX balloon-borne magnetic spectrometer realized a direct measurement of the charge, the velocity, and the rigidity of cosmic rays using plastic scintillators, a high-resolution time-of-flight system, and two silica-aerogel Cerenkov counters in conjunction with a drift chamber/multiwire proportional chamber tracking system. About 75,000 helium isotopes are identified by their mass using the velocity versus magnetic rigidity technique. The measured ^{3}He/^{4}He ratios are corrected to the top of the atmosphere, and a comparison with previous data is given. The observed isotopic composition is found to be generally consistent with the predictions of a standard leaky box model of cosmic-ray transport in the Galaxy.

Subject headings: acceleration of particles — balloons — cosmic rays — nuclear reactions, nucleosynthesis, abundances

1. INTRODUCTION

Most of our knowledge of cosmic-ray propagation in the Galaxy comes from the study of "secondary" species such as Li, Be, and B ($Z = 3$–5) and spallation products of Fe with $21 \leq Z \leq 24$ that are believed to be rare in cosmic-ray sources but relatively abundant in cosmic rays. Thus, from measurements of the energy dependence of ratios such as boron/carbon and subiron/iron, we find that, within the context of the standard leaky box model, the mean free path for escape of heavy nuclei such as CNO and Fe is ~ 12 g cm^{-2} at 2 GeV nucleon^{-1}, decreasing at both lower and higher energies (Garcia-Muñoz et al. 1987; Englemann et al. 1990). The decrease at higher energies is usually interpreted as an energy- (rigidity-)dependent escape probability, while the decrease at lower energies is not understood.

It is important to note, however, that nuclei with $Z \geq 3$ constitute only $\sim 1\%$ of cosmic rays. Hence, it is of great importance to determine the propagation history of the much more abundant H and He nuclei. Among the secondaries of cosmic-ray proton interactions with interstellar H are positrons and antiprotons, both of which are difficult to measure. Because of the relatively large uncertainties in the available measurements and modeling uncertainties (Gaisser & Schaefer 1992), the path length of cosmic-ray protons in the Galaxy is probably only known to within a factor of $\sim \pm 2$, although the most recent measurements are generally consistent with the standard leaky box model and the path length derived from heavier nuclei (Mitchell et al. 1996; Yoshimura et al. 1995; Barwick et al. 1997; Barbiellini et al. 1996).

The rare isotope ^{3}He is produced by interactions of cosmic-ray ^{4}He in the Galaxy, and the ^{3}He/^{4}He ratio is an excellent probe of the propagation history of cosmic-ray ^{4}He. Since ^{3}He is rare in nature (^{3}He/^{4}He $\sim 3 \times 10^{-4}$ in the solar wind), the ^{3}He measured in cosmic rays is believed to be due to breakup of primary ^{4}He. Most satellite and balloon studies of ^{3}He have been at energies from ~ 20 to 200 MeV nucleon^{-1}, well below the maximum in the path length distribution (see reviews in Mewaldt 1986, 1994 and Beatty 1986). While these low-energy results are generally consistent with the path length derived from heavier nuclei, there is considerable scatter with some measurements finding more than the expected amount of ^{3}He (see, e.g., Webber & Yushak 1983).

There have been few measurements of ^{3}He at higher energies. Jordan & Meyer (1984) originally reported a ^{3}He/^{4}He ratio at ~ 10 GeV nucleon^{-1}, which was much greater than expected, but a reinterpretation of this measurement by Webber et al. (1987) suggested a lower value. There have been two recent balloon-borne studies under conditions of maximum solar modulation that extend to ~ 1.5 GeV nucleon^{-1} (Webber, Golden, & Mewaldt 1991; Beatty et al. 1993), both of which report no excess of ^{3}He.

In this paper we report new high-precision measurements of the ^{3}He/^{4}He ratio by the Isotope Matter-Antimatter Experiment (IMAX) from 0.2 to 3.7 GeV nucleon^{-1}, including, for the first time, the region near ~ 2 GeV nucleon^{-1},

[1] Present address: Max-Planck-Institut für extraterrestrische Physik, D-85740 Garching, Germany.
[2] Deceased.

where the path length distribution for CNO is a maximum. We interpret these measurements with standard propagation and solar modulation models, using new cross section data, and pay particular attention to experimental and modeling uncertainties, in order to assess what we can learn about the origin and transport of cosmic-ray ^{4}He.

2. INSTRUMENT CONCEPT AND FLIGHT

The Isotope Matter-Antimatter Experiment (IMAX) shown in Figure 1 is a balloon-borne magnetic spectrometer designed to measure antiprotons and the attendances of light isotopes in the cosmic rays over a wide energy range (Mitchell et al. 1993a). Here we present results on the helium isotopes. For results on the antiproton measurements, we refer to Mitchell et al. (1996).

Particle identification in IMAX is based on the determination of the charge Z, velocity β, and magnetic rigidity R of incident particles. As its basis, IMAX used the NASA/NMSU Balloon-Borne Magnet Facility payload (Golden et al. 1978), consisting of a single-coil superconducting magnet with a set of multiwire proportional chambers, the structural framework, and payload electronics. In order to meet the specific scientific goals, the payload was augmented by a variety of additional detectors and electronics, including a high-resolution time-of-flight system, large-area aerogel Cerenkov detectors, drift chambers for greatly improved trajectory determination, and high resolution scintillation counters.

The rigidity (momentum/charge) is measured using a 61 cm diameter single coil superconducting magnet, providing a magnetic field varying from 0.1 to 2.1 T in the region of the tracking detectors. The tracking system is a combination of drift chambers (DCs) and multiwire proportional chambers (MWPCs). The drift chamber subsystem consists of two identically manufactured drift chamber modules with a hexagonal close-packed structure, which provides 12 measurements in the bending direction (x) and eight in the nonbending direction (y). The average position resolution for helium inferred from residuals to fitted trajectories in the drift chambers is about 65 μm (Hof et al. 1994). The set of eight MWPCs, placed above, below, and between the two drift chamber modules, provides another eight measurements in x and four in y.

Particle trajectories are measured in general with the full hybrid tracking system (DCs plus MWPCs), whereas both tracking subsystems can operate separately in order to provide two independent trajectory measurements. In addition, each single drift chamber module is capable of measuring the trajectory of a charged particle in the field of the magnet. We used this capability for cross checks. The trajectories are reconstructed by means of an iterative numerical fitting algorithm. This algorithm (details in Golden et al. 1991) not only provides the deflection, η, of the incoming particle, which is the reciprocal of the rigidity R, but also the uncertainty in deflection, $\Delta\eta$. The $\Delta\eta$-distribution, shown in Figure 2 for helium particles, actually reflects the quality of the IMAX magnetic spectrometer. This $\Delta\eta$-distribution carries the uncertainty in the tracking (number of measured positions and spatial resolution) as well as the strength of the magnetic field (bending power) along the path of each particle. The maximum detectable rigidity, MDR, is defined as the value at which the uncertainty in the rigidity measurement becomes 100%:

$$\frac{dR}{R} = \frac{R}{\mathrm{MDR}}.$$

The most probable value of $\Delta\eta$ is given by the peak of the $\Delta\eta$-distribution which corresponds to an MDR of 250 GV/c.

Particle velocities were obtained in two energy regimes using different measurement techniques. The energy range from 200 MeV nucleon^{-1} to 1.8 GeV nucleon^{-1} is covered by a high-resolution time-of-flight (TOF) system (Mitchell et al. 1993b; Reimer 1995). Both the bottom and the top TOF arrays consist of three 60 cm × 20 cm × 1 cm Bicron

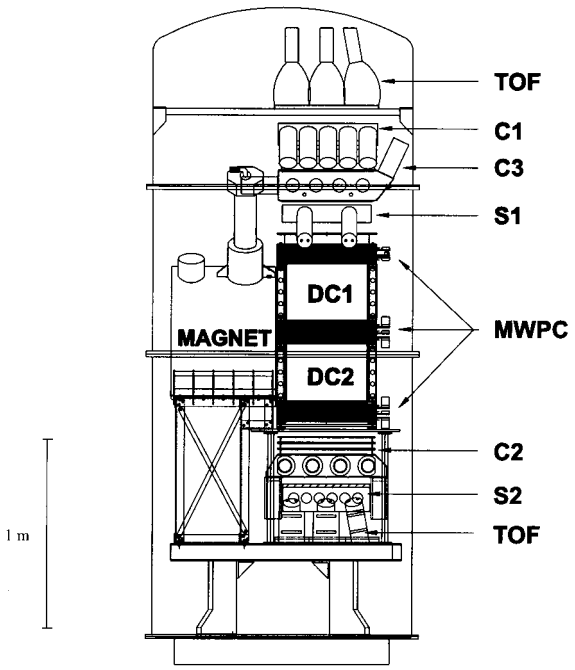

FIG. 1.—The IMAX instrument. TOF is the time-of-flight system, C1 is a Teflon Cerenkov detector, C2 and C3 are the silica aerogel Cerenkov detectors, S1 and S2 are plastic scintilltors, MWPC are three separate sets of multiwire proportional chambers, and DC1 and DC2 are drift chamber modules.

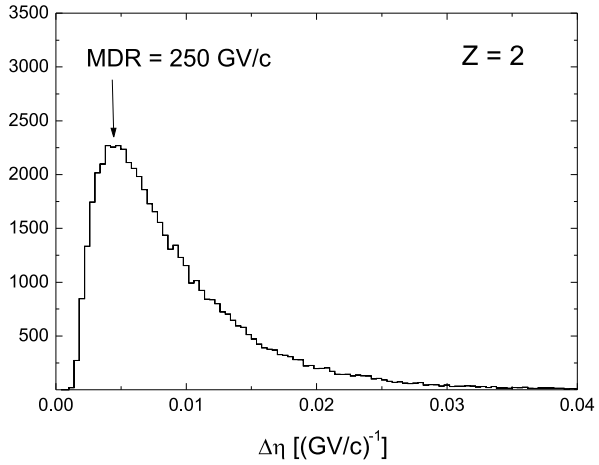

FIG. 2.—The maximum detectable rigidity (MDR) indicated in the distribution of the uncertainty in the deflection measurement for helium nuclei as obtained in IMAX.

BC-420 plastic scintillator paddles, with each paddle viewed by two 2 inch (5 cm) Hamamatsu R2083 PMTs on opposite sides. An average timing resolution of 92 ps was achieved for $Z = 2$, $\beta \simeq 1$ particles between the two separated TOF scintillators over the fully reconstructed curved flight path ($d_{\rm eff}$) of about 2.5 m (see Fig. 3).

In the energy range from 2.5 to 3.7 GeV nucleon^{-1}, two large-area silica aerogel Cerenkov detectors are used to measure particle velocities. These Cerenkov counters (C2 and C3), located above and below the tracking systems, each contain 50 cm × 50 cm × 9 cm of aerogel with refractive index $n = 1.043$ (Labrador et al. 1993; Labrador 1996). The C2 counter is viewed by 14 3 inch (7.6 cm) Hamamatsu R1848 photomultipliers, while C3 is viewed by 16 R1848 photomultipliers. All PMTs are individually pulse-height analyzed. The light yield is obtained on an event-by-event basis with the photoelectron scale based on the 0 and 1 photoelectrons response in each PMT. For $Z = 2$, $\beta \simeq 1$ particles, the light yields from C2 and C3 were about 45 and 50 photoelectrons, respectively. For subsequent analysis, C2 and C3 were mapped, and the signal sum C2+C3 expected from a $Z = 1$, $\beta \simeq 1$ particle was normalized to 1. A third Cerenkov detector (C1) with Teflon radiators ($n = 1.33$) was not used in the current analysis.

The charge determination was performed by four independent ionization energy loss measurements. Besides the two plastic scintillators of the TOF system, which formed the event trigger, two large-area light-integrating counters (S1 and S2) were used to separate particles by charge. S1 contained a 51 cm × 51 cm × 1 cm Bicron BC-400 plastic scintillator, viewed by four 3 inch Hamamatsu R1307 PMTs, and S2 used a 55 cm × 49 cm × 1.8 cm Bicron BC-408 plastic scintillator material, viewed by 12 2 inch Hamamatsu R2409-1 PMTs. The charge was determined using a dE/dx versus β^2 method. The capability of this method is illustrated in Figure 4, which shows the charge separation as obtained from the S2 scintillator.

Doubly charged particles were selected by velocity-dependent rejection of $Z = 1$ and $Z > 2$ particles using the mapped signal of the dE/dx measurements. By combining this power of separation with the other three independent

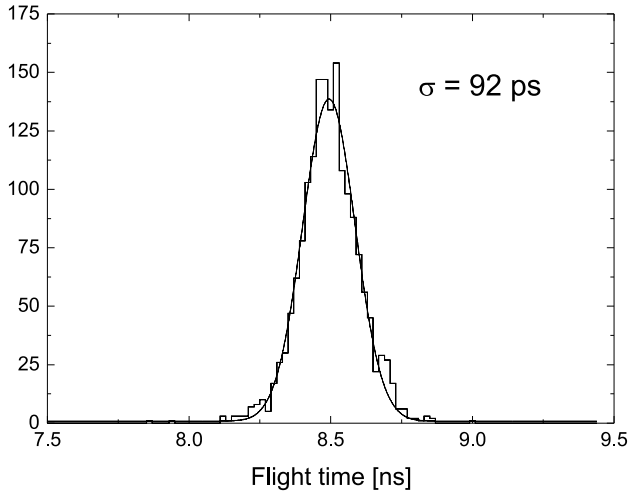

FIG. 3.—Time resolution of the IMAX time-of-flight system for helium isotope measurements. The time resolution shown here represents the actual timing resolution for relativistic helium nuclei along their flight path between the top and the bottom TOF scintillator array.

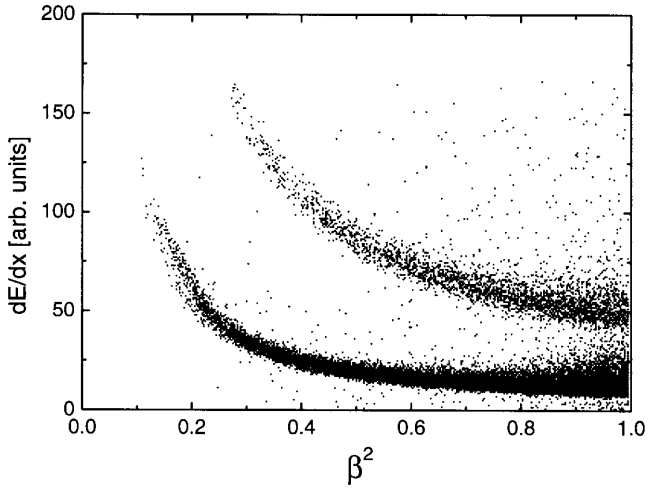

FIG. 4.—Charge separation in the S2 scintillator, one of the four scintillators used in IMAX, illustrated by plotting the ionization energy loss vs. the squared particle velocity. Note that the Landau tail of the proton band is clearly seen at high velocities.

ionization loss measurements, we estimate a charge misidentification probability of less than 4×10^{-6}. This is negligible compared to the statistical uncertainty of the determination of helium isotopic abundances in the IMAX experiment.

The IMAX flight took place on 1996 July 16–17 from Lynn Lake, Manitoba, Canada. The float altitude of 36 km (5 g cm^{-2} of residual atmosphere) was reached about 7 hr after launch. During flight, the latitude varied between 55° 58′ and 57° 40′ north, and the longitude varied between 100° 28′ and 117° 35′. The vertical geomagnetic cutoff rigidity varied between ~0.35 GV at Lynn Lake and 0.63 GV at Peace River. Since these cutoff rigidities correspond to energies of about 70 MeV for protons and 17 MeV nucleon^{-1} for ^{4}He at Lynn Lake and 190 MeV for protons and 52 MeV nucleon^{-1} for ^{4}He at Peace River, the geomagnetic cutoff is well below the instrument cutoff owing to the instrumental grammage in the IMAX experiment and the residual atmosphere on top of the instrument. The data used in the analysis were recorded during the 16 hr flight at float altitude. All payload and detector systems performed well during the flight, and the 2500 kg payload was recovered in excellent shape at Grimshaw near Peace River, Alberta, Canada.

3. DATA ANALYSIS

The acceptance criterion for an event trigger in the IMAX instrument was a fourfold coincidence between the PMT signals from the opposite sides of a top and a bottom TOF scintillator. The following selection criteria were applied to all recorded events to obtain the data set used for the helium isotope analysis:

1. Successful reconstructed particle trajectory with positive deflection.
2. Valid checksum in the event record in order to exclude telemetry transmission errors.
3. Reconstructed particle track completely within the geometry (respective active areas) of all detectors.
4. No appearance of multiple tracks in the tracking system (MWPCs: agreement between delayline readout from opposite sides; DCs: capability of disclosing multiple

tracks by analyzing the pattern signature from triggered drift cells).

5. No appearance of multiple tracks in the TOF arrays (only one paddle hit on top and bottom TOF scintillators).

6. TOF timing position inside the active scintillator area (lightpipe cut) (TOF-TDC internal signature: the difference of the arrival time (TDC) obtained at each end of a TOF scintillator gives a position where the particle hits the detector.)

7. Internal agreement of the TOF timing signal within a 3 σ range (TDC vs. ADC correlation of an event: the arrival time [TDC] as well as the ionization loss measurement [ADC] obtained at each end of a TOF scintillator gives a position where the particle hits the detector).

8. Agreement within 3 σ of the position in both top and bottom TOF scintillators determined by the TOF PMTs (timing difference) with the position determined by the reconstructed trajectory.

9. Fourfold agreement in charge determination using the four independent ionization energy-loss measurements.

For analyzing helium isotopes in the higher energy regime using the aerogel Cerenkov detectors, additional cuts were applied to the data. These cuts assure high-quality data selections by taking advantage of having two aerogel Cerenkov detectors of similar characteristics and two independent velocity measurements above 2.55 GeV nucleon^{-1}:

10. Agreement between the map-normalized light yields of C2 and C3 by setting a lower limit of 0.1 on the relative correlation probability.

11. Agreement between the map-normalized light yields of C2 + C3 and the velocity measured by the time-of-flight system above $\beta > \sim 0.95$.

12. Threshold in the map-normalized light yield of C2 and C3 > 0.24.

The efficiency statistics of the selection criteria given in Table 1 show two columns: the efficiency for each individual cut applied to the data, and the running fraction roughly in the order in which the cuts were applied during the analysis. Often, more than one individual cut rejects a particular event. These dependencies between different cuts explain the difference between the fraction of events by applying an individual cut and the running fraction of the cuts.

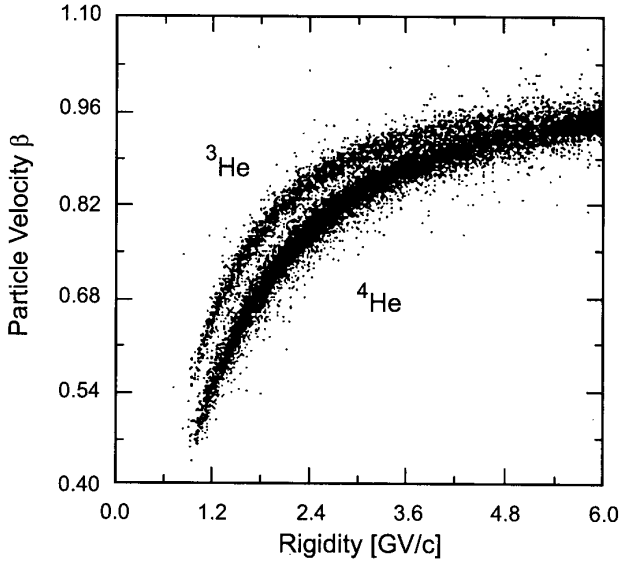

FIG. 5.—Velocity-rigidity separation of the helium isotopes obtained using the time-of-flight system for determination of the particle velocity.

Figure 5 shows the separation of the helium isotopes in a rigidity-velocity plot using the TOF system, while Figure 6 illustrates the separation using the aerogel Cerenkov counters as velocity detectors. The ^{3}He and ^{4}He isotopes are well separated in both operating modes in the energy ranges considered for the analysis.

Finally, the mass of each particle was directly determined using the relation

$$m = \frac{RZe}{\gamma\beta c}, \tag{1}$$

where R is the magnetic rigidity, β is the particle velocity, $Z \times e$ is the particle charge, and γ stands for the Lorentz factor. In Figure 7 we show for a particular energy the mass histograms of the helium isotopes obtained by applying different cuts on the data. This figure demonstrates the sensitivity of the instrument response to different tight cuts.

The χ^2 cut reflects the quality of the particle track reconstruction based on the χ^2 from the fitting algorithm, the $\Delta\eta$ cut is a cut in the distribution of the deflection uncertainty and reflects the quality of the magnet spectrometer depend-

TABLE 1

SELECTION CRITERIA STATISTICS FOR THE IMAX DATA USED FOR THE HELIUM ISOTOPE ANALYSIS

	INDIVIDUAL CUT		RUNNING FRACTION	
SELECTION CRITERION	Events	Percentage (%)	Events	Percentage (%)
Appropriate trajectory with R > 0	1568115	100	1568115	100
Trajectory inside detector geometry	1107827	70.6	1107827	70.6
No multiple trajectories	1428563	91.1	1042376	66.5
Single TOF paddle hit	1366369	87.1	962299	61.4
TOF light pipe cut	1461721	93.2	947267	60.4
TOF TDC position vs. ADC position	1413215	90.1	922380	58.8
TOF TDC position vs. trajectory fit	996673	63.6	826840	52.7
Charge agreement	1083215	69.1	See next row	
Charge selection Z = 2	73117	4.7	56919	3.6
N_x, N_y	1123681	71.7	50634	3.2
χ_x^2, χ_y^2	1423981	90.8	47809	3.0
$\Delta\eta$	1485128	94.7	47650	3.0
β (TOF) vs. β (Cher.)	1012901	64.6	47647	3.0
Light yield agreement C2 vs. C3	1031263	65.7	47598	3.0
Cerenkov threshold applied	Not individually applicable		10390	0.7

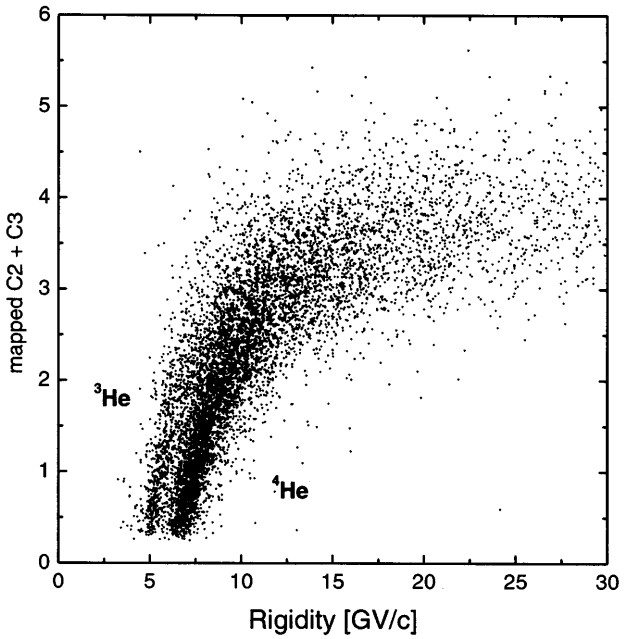

FIG. 6.—Velocity-rigidity separation of the helium isotopes using the silica aerogel Cerenkov detectors for determination of the particle velocity. Events were selected above a threshold of five photoelectrons in each aerogel Cerenkov counter, which corresponds to an energy of 2.55 GeV nucleon^{-1}.

ing on the actual magnetic field strength and the achieved spatial resolution, and N_x and N_y are the numbers of detector layers in the tracking system (x and y readout) used as input for the track reconstruction algorithm.

The improvement in mass resolution obtained using tighter cuts can clearly be seen and illustrates the inherent capability of IMAX to separate isotopes. Figure 7*a* provides a mass resolution of 0.2 amu. Thus, determining isotope abundance ratios under the condition of tight cuts would be an easy task. But from a careful and systematic analysis of these data, we found that tight cuts that improve the mass resolution can introduce a bias in the abundance ratio. This is an important aspect in the data analysis of IMAX and obviously a characteristic feature of magnetic spectrometers in general. For that reason we explicitly show this effect in Figure 8.

In this figure for a given rigidity or mass bin the following ratio is shown: number of events after being influenced by the specific cut divided by the number of events prior to the cut. Note that this ratio depends on the tightness of the χ^2 cut on the tracking and, more importantly, that it becomes rigidity dependent. As a result, the cut introduces a bias in the ^{3}He/^{4}He ratio since ^{3}He and ^{4}He at a given energy nucleon^{-1} have different rigidities. We attribute this effect to the Coulomb scattering process. The lighter isotope is more subject to χ^2 tracking cuts than the heavier one. In order to assure high-quality particle tracking and to avoid biasing the helium isotope ratio, only the following moderate selection criteria were applied to the data in addition to the general event selection criteria listed above:

13. A minimum of 13 hit wires (N_x) were used to fit the track in x (of 20); a minimum of seven hit wires (N_y) were used to fit the track in y of 12).
14. χ^2 for a reconstructed trajectory ≤ 8 in both x and y.
15. $\Delta\eta$ for a reconstructed track ≤ 0.04 ($\equiv$MDR ≥ 25).

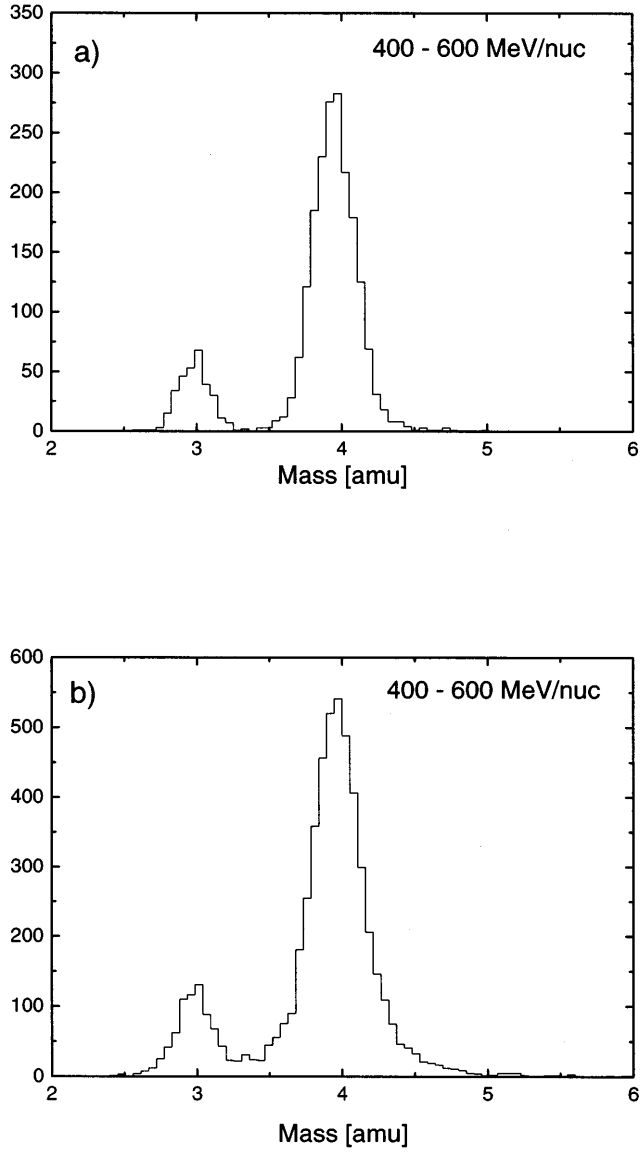

FIG. 7.—Helium isotope mass resolution achieved in the 400–600 MeV nucleon^{-1} energy range (*a*) by applying tight tracking cuts ($\chi^2 < 5$, $\Delta\eta < 0.007$, $N_x > 14$, $N_y > 8$) or (*b*) by applying tracking cuts actually chosen for the helium isotope analysis ($\chi^2 < 8$, $\Delta\eta < 0.04$, $N_x > 13$, $N_y > 7$). The full inherent isotope mass separation quality of IMAX illustrated in (*a*) was not used for determination of the helium isotope ratio because tight tracking cuts do influence the value of the ^{3}He/^{4}He ratio. Thus, loose cuts (*b*) have been chosen for the subsequent analysis.

These loose cuts, however, lead to mass histograms that partially overlap and that are not Gaussian in shape, as shown in Figure 7*b*. Under these conditions, the analysis becomes more complicated. In order to derive accurate isotope ratios, we developed an instrument response model to simulate accurately the complete performance of the IMAX instrument on an event-by-event basis. This model is not a full Monte Carlo program because it is based in part on characteristic distributions of detector responses as input to the simulation, which we obtained empirically from the instrument. These were (1) the $\Delta\eta$ distributions representing the magnetic spectrometer in different rigidity regimes, obtained from the fitting algorithm explained above; (2) the β distribution of the incoming particles, which represent their spectral shape; and (3) the uncertainty

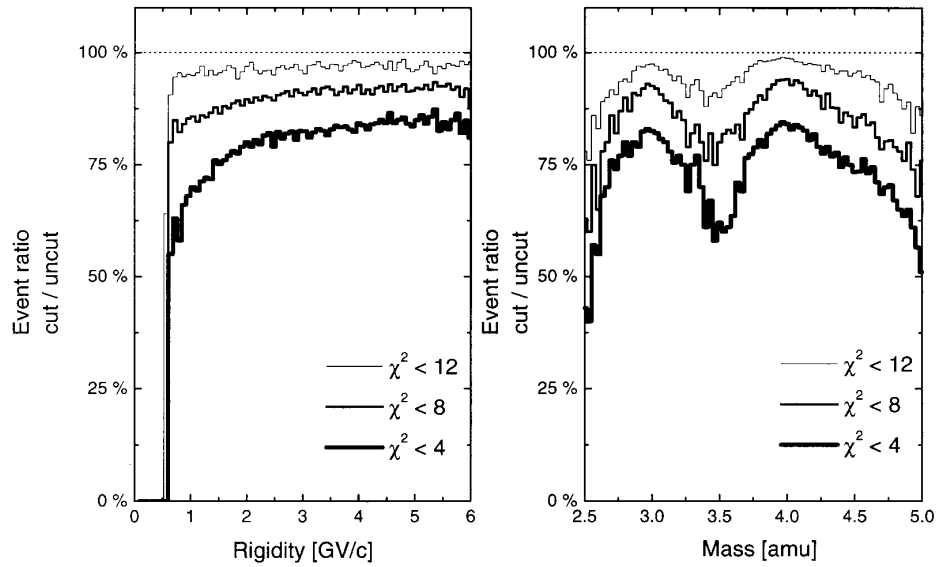

FIG. 8.—Influences of various tracking cuts on the data. The figures are obtained by dividing a data set after applying the indicated cut by the noninfluenced data set, separated in bins over the rigidity and the isotope mass, respectively. The percentage of the event ratio directly reflect the cut efficiency.

($\Delta\beta$) in the velocity measurement. In the TOF regime, the resolution $\Delta\beta$ is determined by the timing error (Δt) and in the Cerenkov range primarily by the number of photoelectrons involved in a measurement. In the TOF regime, we also took into account the nine possible event trigger combinations, which contribute differently to the overall time resolution shown in Figure 3. In the Cerenkov regime, the contribution of knock-on electrons, the scintillation light background to the signal amplitude, as well as nonuniformities in the refractive index of the silica aerogel material were included in the analytical simulation of the instrument performance.

This model simulated on an event-by-event basis the rigidity and the velocity of incoming particles that IMAX would provide in a real measurement. Using a sufficiently large number of events and an assumed ^{3}He/^{4}He ratio as input, smooth mass distributions were obtained that were then normalized to the number of events observed in the specific energy bin. Each analyzed mass distribution was fitted by the use of a χ^2 minimization procedure, which varied the initial ^{3}He/^{4}He ratio and compared the simulated and measured mass histograms. The chosen minimization function was

$$\chi^2 = \sum_{i=1}^{\text{maxbin}} \frac{(N_i - n_i)^2}{\sigma_i^2} \quad \text{with} \quad \sigma_i^2 = \sqrt{n_i}\,,$$

where N_i is the (renormalized) number of events in the ith bin of the simulation and n_i is the number of events observed in the ith bin of the data histogram. The appropriate ^{3}He/^{4}He ratio for a measured mass histogram is the ratio of the model that corresponds to the minimal χ^2 value.

Using this approach, we found that the simulated mass resolution based on the inputs given above turned out to be systematically somewhat better than in the real measurement, particularly at low energies. We attribute this effect to multiple scattering of the particles, based on the following arguments.

Theoretically, there are three independent contributions to the mass resolution in a magnet spectrometer similar to IMAX: the bending power of the magnetic spectrometer coupled with the intrinsic limits of spatial resolution which the tracking detectors provide, the precision of the velocity measurement (given either by timing or by the number of Cerenkov photoelectrons), and last but not least, the multiple scattering of the particle along its path in the bending area of the magnet. These three independent contributions can be expressed by the following equation:

$$dm = m\sqrt{\gamma^4\left(\frac{d\beta}{\beta}\right)^2 + \left(\frac{R}{\text{MDR}_{\text{spec}}}\right)^2 + \left(\frac{R}{\text{MDR}_{\text{coul}}}\right)^2}\,, \tag{2}$$

where γ is the Lorentz factor, $d\beta/\beta$ is the relative error in the velocity measurement, $R/\text{MDR}_{\text{spec}}$ stands for the contribution solely given by the magnetic spectrometer, and the last term stands for multiple coulomb scattering.

Our IMAX instrumental simulation, however, did not incorporate a separate term for multiple Coulomb scattering. In a given rigidity regime, the $\Delta\eta$ distribution, as obtained by the fitting algorithm, was the only representative of the last two terms of equation (2). This derived $\Delta\eta$ distribution obviously does not fully represent the contributions of the last two terms: the analytical reconstruction of trajectories by solving the equation of motion for a particle in a nonhomogeneous magnetic field as it traverses different layers of material will not describe multiple Coulomb scattering in its full strength. Because a track reconstruction algorithm works by finding a single smooth particle trajectory in order to determine its curvature and expresses it in the value of the magnetic rigidity R, it will inevitably smooth the trajectory of multiple-scattered events during the fitting process. This provides a $\Delta\eta$ distribution that does not adequately describe the real measurement accuracy at low energies. With this understanding in mind, we assumed that the last two terms of equation (2) can be expressed by an effective MDR_{eff}:

$$\left(\frac{R}{\text{MDR}_{\text{eff}}}\right)^2 = \left(\frac{R}{\text{MDR}_{\text{spec}}}\right)^2 + \left(\frac{R}{\text{MDR}_{\text{coul}}}\right)^2. \tag{3}$$

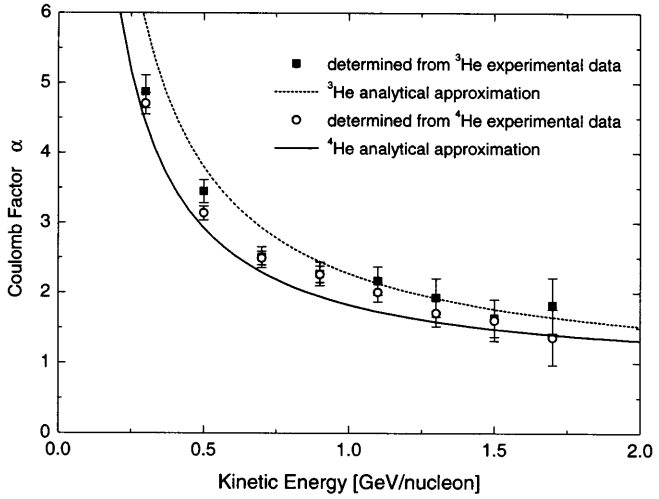

FIG. 9.—The Coulomb factor α for ^{3}He and ^{4}He. Data points were determined from the measured helium nuclei. The curves show the analytical approximation using the multiple Coulomb scattering formula applied to the actual instrumental grammage in the IMAX experiment.

The MDR_{spec} values that represent the magnetic spectrometer can be obtained empirically to a very good approximation directly from high-energy helium nuclei where the multiple scattering effect becomes negligible.

The MDR_{spec} derived from the high-energy data can be related to the effective MDR_{eff} by applying a simple scaling factor, α:

$$MDR_{eff} = \frac{MDR_{spec}}{\alpha} .$$

The factor α is expected to be close to 1 at high energies and to increase at lower energies, which reflects the increase of multiple scattering. We call α the Coulomb factor and use it as a free parameter in our simulation, giving a total of two free parameters for the simulation (the ^{3}He/^{4}He ratio and the Coulomb factor). In principle, these parameters can be found simultaneously, but we chose an iterative process. Starting with a reasonable assumption for the ^{3}He/^{4}He ratio, we found the Coulomb factor by means of χ^2 minimization. Because of their different masses ^{3}He and ^{4}He nuclei suffer different multiple scattering at the same energy. Therefore, we determined separate Coulomb factors for both isotopes.

With these optimized Coulomb factors we again fitted the ^{3}He/^{4}He ratio, as described above. The resulting ^{3}He/^{4}He ratio value can be used as input for the further improvement of α in an iteratative way. In practice, this procedure quickly converged after two iterations.

In Figure 9 we show the derived Coulomb factors for different energies along with two curves that represent the analytic determination of equation (2) by using explicitly the Coulomb contribution. Following geometrical considerations of a trajectory in a magnetic spectrometer (Golden et al. 1973), the sagitta s is determined by

$$s = \frac{L^2 B}{8R} ,$$

and the uncertainty in the sagitta ds caused by Coulomb scattering is given by

$$ds_{Coul} = \frac{1}{4\sqrt{3}} L\Theta_{Coul}^{plane}$$

with

$$\Theta_{Coul}^{plane} = \frac{13.6 \text{ MeV}}{\beta cp} Z\sqrt{\frac{L}{X_0}}\left(1 + 0.0038 \ln \frac{L}{X_0}\right)$$

(Barnett et al. 1996), where L is the radiation length, X_0 is the grammage of the material along the particle's trajectory in the bending area of the magnet, and Θ_{Coul}^{plane} is the projected deflection angle. The Coulomb term from equation (2) is therefore

$$\frac{R}{MDR_{Coul}} = \frac{8}{4\sqrt{3}} \frac{13.6 \text{ MeV}}{0.3BL\beta} \sqrt{\frac{L}{X_0}}\left(1 + 0.0038 \ln \frac{L}{X_0}\right),$$

where $B \times L$ is in a more general view the magnetic field integral $\int B\, d\ell$ of $\sim$0.3 Tm in IMAX.

By this procedure one can reach the best fit between the simulated mass distribution and the measured one. As an example we show this comparison in Figure 10. The very good agreement between the simulated smooth mass distribution and the histogram as measured by the IMAX instrument is very satisfactory.

The general agreement between these calculated curves and the empirically derived Coulomb factors (Fig. 9), along with the good agreement between simulated and measured mass distributions shown in Figure 10, indicate that we have accurately simulated the physical processes involved. The uncertainty in determining the exact value of α contributes only in an inferior way to the final uncertainties in the ^{3}He/^{4}He ratio that, at higher energies in the TOF regime, is dominated by the TOF resolution.

The fitted ^{3}He/^{4}He ratios for all analyzed energy bins from 200 MeV nucleon^{-1} to 1.8 GeV nucleon^{-1} (TOF regime) and from 2.55 GeV nucleon^{-1} to 3.66 GeV nucleon^{-1} (Cerenkov regime) are given in Table 2. The uncertainty in the ^{3}He/^{4}He ratio is directly determined from the 1 σ uncertainty in the χ^2 statistics of the fitting procedure.

4. PROPAGATION TO THE TOP OF ATMOSPHERE

In order to compare our results with those of previous experiments or with predictions of models of cosmic-ray transport in the Galaxy, we first corrected for the effects of the instrument and atmospheric overburden on the ^{3}He/^{4}He ratios. The corrections were calculated from the results of a cosmic-ray transport code. Since there was a significant amount of material above the tracking volume of IMAX ($\sim$12 g cm^{-2} of instrument material and 5 g cm^{-2} of atmosphere), the corrections were important, and the inputs to the calculation were considered carefully.

The most important inputs are mass-changing cross sections for ^{3}He and ^{4}He and cross sections for production of ^{3}He from spallation of ^{4}He above the IMAX tracking volume. Figure 11 shows mass-changing cross sections for ^{4}He on carbon and aluminum targets.

These cross sections were parameterized using the formula

$$\sigma_{^4\text{He}-\delta A \geq 1} = 10\pi(1.075A_T^{0.355} + 1.4)^2 \times [1 - 0.62 \exp(-E/200) \sin(10.9E^{-0.28})] , \quad (4)$$

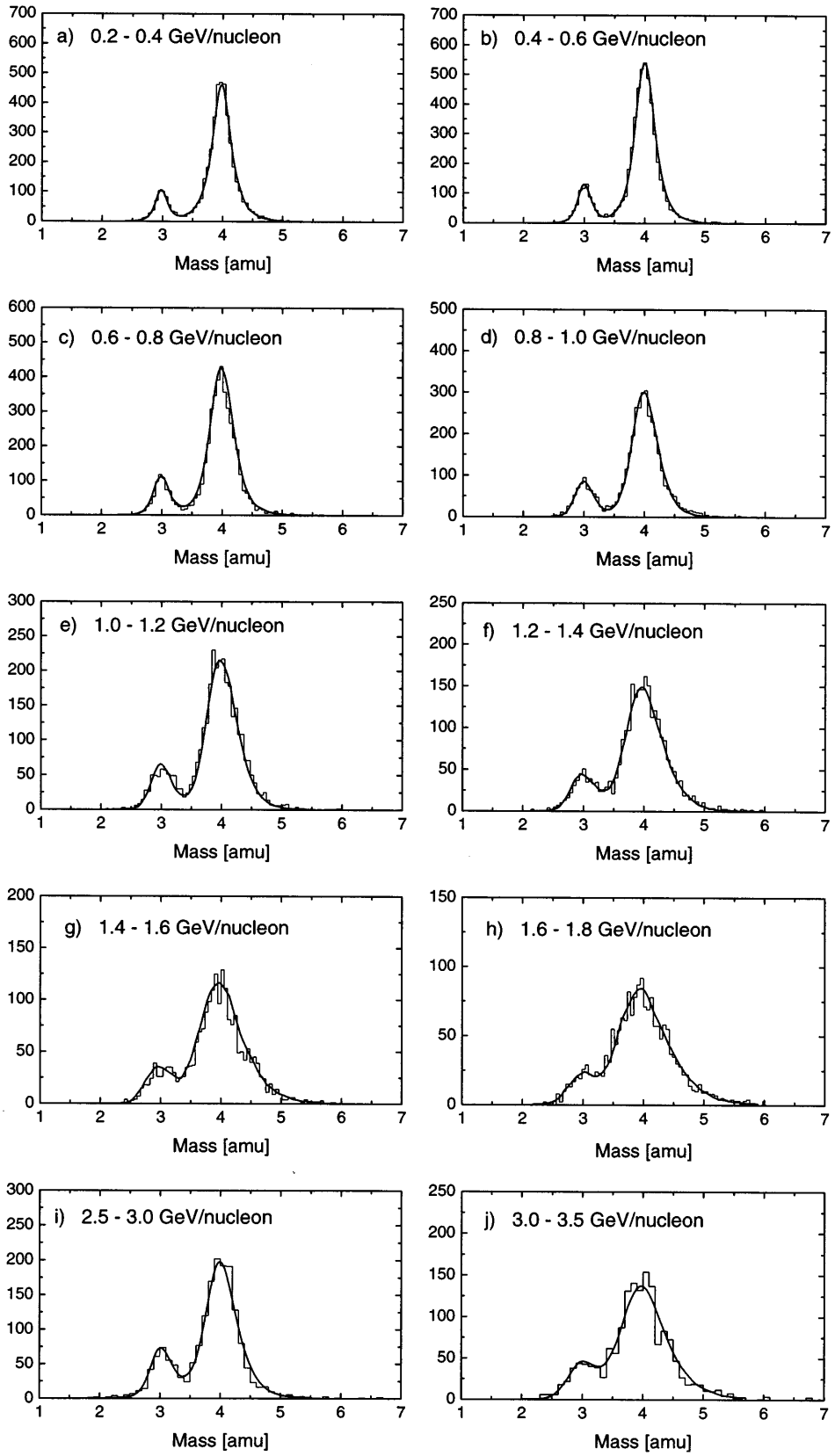

FIG. 10.—Mass histograms and appropriate fits of the helium isotopes from 0.2 to 3.7 GeV nucleon^{-1}. The data from (*a*) to (*h*) were obtained with the time-of-flight system for the particle velocity measurement, whereas (*i*) and (*j*) made use of the aerogel Cerenkov detectors for measuring the particle velocity. The instrumental simulation represents the most probable ratio of ^{3}He/^{4}He in the specific energy interval.

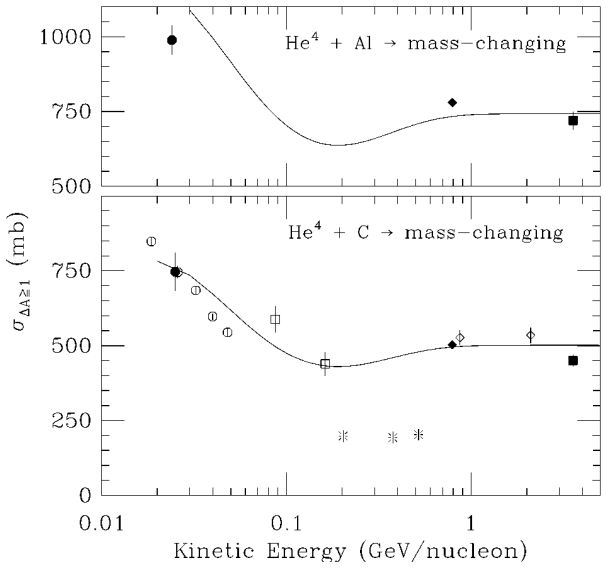

FIG. 11.—^{4}He mass-changing cross sections on carbon and aluminum targets, with our parameterization of the data. Data points are as follows: *filled circles*, Dubar et al. (1989); *filled diamonds*, Tanihata et al. (1985); *filled squares*, Aksinenko et al. (1980); *open circles*, Auce et al. (1994); *open squares*, DeVries et al. (1982); *bursts*, Webber (1990); *open diamonds*, Jaros et al. (1978).

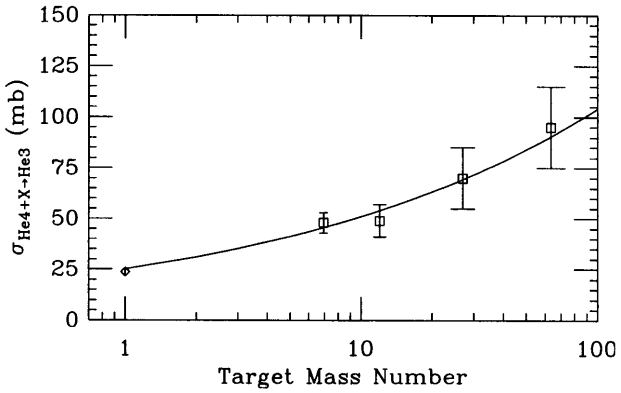

FIG. 12.—High-energy cross sections for production of ^{3}He from ^{4}He fragmentation on various targets. Also shown is our $A_T^{0.31}$ parameterization. Data points are as follows: *squares*, Abdurakhimov et al. (1981), 3.6 GeV nucleon^{-1}; *diamond*, Glagolev et al. (1993), 2.59 GeV nucleon^{-1}.

where A_T is the mass number of the target nucleus, and E is the kinetic energy of the projectile, in MeV nucleon^{-1}. The energy-dependent term was adopted from Letaw, Silberberg, & Tsao (1983).

The measurements by Webber et al. at $\sim$0.2–0.5 GeV nucleon^{-1} are systematically lower than the trend of the other measurements by a factor of $\sim$2. They are also systematically lower than simple geometrical estimates of the cross section (Tanihata et al. 1985; Sihver et al. 1993). We have therefore chosen to disregard these data in our parameterization in favor of the other available measurements.

There are very few measurements of the ^{3}He mass-changing cross section in heavy targets. However, Tanihata et al. (1985) have measured mass-changing cross sections for both ^{3}He and ^{4}He in carbon and aluminum targets. They find the ^{3}He cross section to be 10% greater than that of ^{4}He for both targets, consistent with electron-scattering measurements of the charge radii of ^{3}He and ^{4}He (Barrett & Jackson 1977, p. 146). We have therefore set the ^{3}He mass-changing cross sections to be 10% greater than those of ^{4}He in our calculations. These parameterizations lead to a path length in air of 40 g cm^{-2} for ^{3}He and 44 g cm^{-2} for ^{4}He at high energies.

For production of ^{3}He from spallation of ^{4}He in the atmosphere and instrument, we used the cross sections on a hydrogen target of Webber (1990), Abdullin et al. (1994), Bizard et al. (1977), and Glagolev et al. (1993), scaled to heavier targets using a scaling factor of $A_T^{0.31}$. The scaling factor was calculated from a fit to high-energy cross section data from Abdurakhimov et al. (1981), shown in Figure 12.

Other cross section inputs included mass-changing and spallation cross sections for heavier cosmic rays ($Z > 2$) in the atmospheric overburden, compiled from Kruger & Heymann (1971), Olsen et al. (1983), Webber et al. (1990c), and Sihver et al. (1993). However, our data selection criteria vetoed cosmic rays with $Z > 2$ at the top of the instrument, so corrections to the ^{3}He/^{4}He ratio resulting from heavy cosmic rays were only necessary for the 5 g cm^{-2} of residual atmosphere above the instrument.

We also included in our calculations an estimate of the multiplicity of charged pions produced in the interaction ^{4}He + target $\rightarrow$ ^{3}He + X. If this interaction occurred above the tracking volume, and charged pions were produced along with the ^{3}He, anomalous signals would have been registered in the scintillators and/or tracking systems, and the event would have been vetoed, thus resulting in no increase in the measured ^{3}He flux. This effect becomes important above the kinetic energy threshold $\sim$ 0.2 GeV nucleon^{-1}, and at 2.6 GeV nucleon^{-1} about 44% of interactions producing ^{3}He are accompanied by charged pions (Glagolev et al. 1993).

In the computer code, the atmosphere and instrument materials were treated as thin slabs, and the flux of a particular cosmic-ray species $J_i(E)$ at depth x was obtained by solving numerically:

$$J_i(E, x) = J_i(E_i, x - \Delta x)\,\frac{\omega_i(E_i)}{\omega_i(E)}\left(1 - \frac{\Delta x}{\lambda^i_{\rm int}}\right) + \sum_{k \geq i} \frac{\omega_k(E_k)}{\omega_k(E)}\, J_k(E_k, x - \Delta x)\left[\frac{\Delta x}{\lambda^{ki}_{\rm spall}(E)}\right], \quad (5)$$

where E_i is the energy of a nucleus of species i at path length $(x - \Delta x)$ such that its energy at path length x is E, $\omega_i(E)$ is the mean energy loss per unit path length, $\lambda^i_{\rm int}$ is the inelastic mean free path, and $\lambda^{ki}_{\rm spall}$ is the mean free path for species k to spallate into species i (Protheroe et al. 1981).

The transport code was run iteratively, changing the input TOA ^{3}He and ^{4}He spectra until the propagated spectra and ^{3}He/^{4}He ratios calculated by the code matched the measured IMAX data. The results of the calculation were then used to calculate energy-dependent TOA correction factors for the IMAX ^{3}He/^{4}He ratios.

The transport code was also used to calculate the sensitivity of the corrections to the uncertainties in the cross sections (assumed to be $\sim$10%). The code was run a large number of times, each time perturbing the cross sections by a Gaussian deviate. Each run resulted in slightly different corrected TOA isotope ratios. The standard deviation of the distribution of these different corrected ratios was 0.007, independent of energy, and was added in quadrature to the

TABLE 2

IMAX ^{3}He/^{4}He Ratios and Ratios Corrected to Top of Atmosphere

Instrument		Top of Atmosphere	
Energy Ratio (MeV nucleon^{-2})	^{3}He/^{4}He	Energy Ratio (MeV nucleon^{-2})	^{3}He/^{4}He
200–400	0.154 ± 0.007	255–440	0.127 ± 0.01
400–600	0.168 ± 0.007	440–634	0.146 ± 0.01
600–800	0.181 ± 0.008	634–831	0.162 ± 0.011
800–1000	0.212 ± 0.010	831–1029	0.194 ± 0.013
1000–1200	0.206 ± 0.010	1029–1229	0.190 ± 0.013
1200–1400	0.207 ± 0.012	1229–1428	0.192 ± 0.015
1400–1600	0.220 ± 0.014	1428–1628	0.205 ± 0.016
1600–1800	0.198 ± 0.015	1628–1828	0.186 ± 0.017
2550–3020	0.245 ± 0.017	2578–3048	0.234 ± 0.019
3020–3660	0.218 ± 0.017	3048–3688	0.206 ± 0.019

statistical errors of the measured isotope ratios. An additional energy-dependent uncertainty in the ratio was added in quadrature to reflect our uncertainty in the efficiency with which the IMAX detectors veto ^{4}He interactions that produce charged pions along with ^{3}He. This uncertainty in the ^{3}He/^{4}He ratio increases with increasing energy and has a magnitude of 0.006 at 3 GeV nucleon^{-1}.

Table 2 lists the measured ^{3}He/^{4}He ratios and the ratios corrected to TOA. The correction factors ranged from 0.825 at the lowest energy bin to 0.945 at the highest energy bin.

5. INTERPRETATION AND DISCUSSION

5.1. *Propagation Model*

To test the hypothesis that the origin and propagation history of Galactic cosmic-ray (GCR) helium is identical to that of heavier GCRs, we have compared our TOA ^{3}He/^{4}He measurements with the predictions of an interstellar propagation model that accurately reproduces the observed B/C secondary-to-primary ratio. We use a steady state leaky box model based on the formalism of Meneguzzi, Audouze, & Reeves (1971), described previously in Leske (1993) and Krombel & Wiedenbeck (1988). The model includes the effects of escape from the Galaxy, energy losses in and nuclear interactions with the interstellar medium (ISM), and decay of radioactive species. The increased energy loss due to the ionized fraction of hydrogen in the ISM is accounted for as in Soutoul, Ferrando, & Webber (1990), and the ISM is assumed to be 90% hydrogen and 10% helium by number. The source spectra for all GCRs are taken to be power laws in momentum per nucleon, with an index of -2.35 ($dJ/dE \propto p^{-2.35}$), and the source elemental abundances are taken from the *HEAO 3* C-2 analysis of Englemann et al. (1990). The mass-changing and partial cross sections for GCRs with $Z > 2$ are taken from Webber, Kish, & Schrier (1990a, 1990b, 1990c, and 1990d) and Ferrando et al. (1988). The cross sections for helium are discussed in detail below.

5.2. *GCR Path Length Distribution*

In order to use the model to make predictions for the ^{3}He/^{4}He ratio, we must use as input an appropriate path length distribution (PLD) for GCRs in the galaxy. Generally, the PLD is found by fitting the predictions of the propagation model to measurements of the B/C ratio. Since boron can reasonably be assumed to be absent in the GCR sources, the model then gives a measure of the effects of propagation in the ISM. Assuming ^{4}He has a propagation history similar to that of other primary GCRs, we can use the model to predict the flux of secondary ^{3}He and hence the ^{3}He/^{4}He ratio.

For this work, we have not attempted to fit a path length to the B/C data ourselves. Rather, we use the PLD derived by Webber et al. (1996), who have incorporated into their propagation calculations newly measured cross sections relevant to the propagation of GCR B, C, N, and O. Their best fit is a pure-exponential PLD with an energy-dependent mean path length given by $\lambda_e = 31.6\beta R^{-0.60}$ g cm^{-2} for rigidities greater than 4.7 GV, and $\lambda_e = 12.5\beta$ g cm^{-2} for lower rigidities. Using this λ_e, we find that our propagation model reproduces the low-energy *Voyager 2* and *ISEE* 3 B/C measurements (Webber et al. 1996; Krombel & Wiedenbeck 1988) and the high-energy *HEAO 3* C-2 measurements (Englemann et al. 1990) to better than 6% over the energy range from $\sim$0.1 to $\sim$30 GeV nucleon^{-1}. Since the newly measured cross sections used in Webber et al. (1996) will have a negligible effect on ^{3}He/^{4}He predictions, we have therefore adopted their PLD for use in our model.

However, several other authors have calculated different PLDs from fits to the B/C data, using similar leaky box assumptions and ISM composition (Ferrando et al. 1991; Heinbach & Simon 1995; DuVernois, Simpson, & Thayer 1995). It is not clear whether the differences in these fits are due to the cross section inputs or to differing implementations of the leaky box model. To account for these differences, we have incorporated into our propagation model a ±15% uncertainty in λ_e. We discuss below the contribution of this, and other input uncertainties, to the uncertainty in the ^{3}He/^{4}He prediction of our model.

5.3. *Helium Cross Sections*

We now describe the cross section inputs to the model relevant to the propagation of helium in the ISM. Figure 13 shows ^{3}He and ^{4}He mass-changing cross sections on a hydrogen target, along with our parameterizations of the data. Also shown are the ±10% error bands we assign to the cross sections in the propagation model. These cross sections were scaled by a factor of 2.36 to obtain cross sections on ^{4}He in the ISM (Jaros et al. 1978; Lloyd-Owen et al. 1986).

Figure 14 shows cross section data for production of ^{3}He from ^{4}He on a hydrogen target. Since GCR ^{3}H decays into ^{3}He with a short half-life (12.26 yr), we have combined the ^{3}He and ^{3}H production cross section data in the figure. Lebowitz & Miller (1969) measured only the ^{3}H production cross section, so we have combined their measurement with the average of the ^{3}He measurements of Glagolev et al. (1993). Since there are few measurements and they exhibit little structure, our model uses a constant 54 mb parameterization of the cross section with a ±10% error band, as indicated in the figure. For ^{4}He on ^{4}He reactions in the ISM, this cross section was scaled by a factor of 1.52 ± 0.3 (Hirzebruch et al. 1993). The figure also shows the semi-empirical prediction for this cross section adopted by Meyer (1972). Meyer's cross section has been used by several authors in GCR helium propagation calculations (see, e.g., Webber & Yushak 1983; Mewaldt 1986), but it is inconsistent with the recent cross section measurements.

Partial cross sections for production of ^{3}He/^{4}He from heavier GCRs were compiled from Kruger & Heymann (1973) and Olsen et al. (1983).

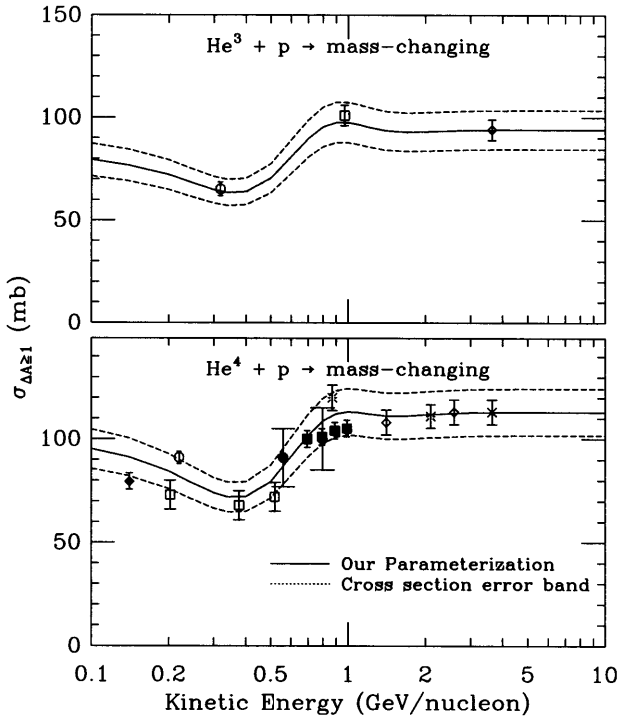

FIG. 13.—^{3}He and ^{4}He mass-changing cross sections on a hydrogen target, along with our parameterizations of the data. The dashed lines show the $\pm 10\%$ error band assigned to the cross sections in the propagation model. Data points for the ^{3}He cross section are as follows: *circle*, Blinov et al. (1985); *square*, Blinov et al. (1984); *diamond*, Glagolev et al. (1993). Data points for the ^{4}He cross section are as follows: *filled diamond*, Nicholls et al. (1972); *open circle*, Abdullin et al. (1994); *open squares*, Webber (1990); *filled circles*, Klem et al. (1977); *filled squares*, Velichko et al. (1985); *bursts*, Jaros et al. (1978); *open diamonds*, Glagolev et al. (1993); *cross*, Ableev et al. (1982). Note: filled symbols indicate inelastic cross sections for protons on a helium target.

5.4. *Solar Modulation*

We account for the effect of solar modulation on the GCR fluxes using the spherically symmetric approach of Fisk (1971), which includes diffusion, convection, and adiabatic deceleration of GCRs in the outward-flowing solar wind.

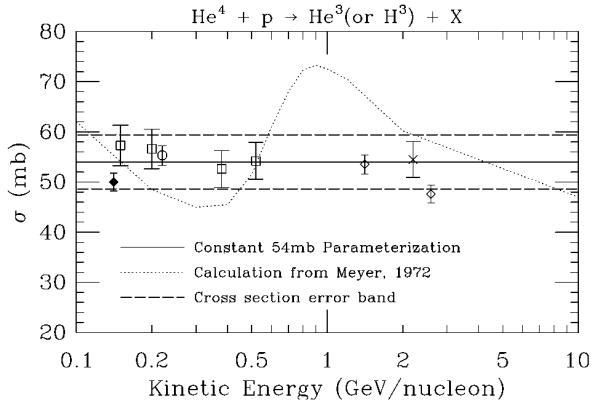

FIG. 14.—Cross sections for production of ^{3}He from ^{4}He on a hydrogen target, including tritium decay, along with our parameterization of the data. The dashed lines show the $\pm 10\%$ error band assigned to this cross section in the propagation model. The cross section adopted by Meyer (1972) is also shown. Data points are as follows: *filled diamond*, Nicholls et al. (1972); *squares*, Webber (1990); *circle*, Abdullin et al. (1994); *cross*, Lebowitz & Miller (1969); *open diamonds*, Glagolev et al. (1993).

The form for the diffusion coefficient is taken to be $\kappa(R) = \kappa_0 \beta R$, where R is the rigidity and β is the velocity of the cosmic ray. The diffusion coefficient is assumed to be independent of position within the heliosphere. With this form for κ, the level of solar modulation at radius R_0 can be characterized by the parameter $\phi = SV_s(R_b - R_0)/3\kappa_0$.

The level of solar modulation appropriate for the time of the IMAX flight was found by fitting modulated helium spectra from the propagation model to *IMP-8* data (W. McGuire, P. Schuster, & F. McDonald 1995, private communication with A. Davis) for the same time period and to a preliminary IMAX helium spectrum. The level was found to be $\phi = 750 \pm 100$ MV, which is consistent with the value determined from the IMAX proton data (Mitchell et al. 1996).

5.5. *The* ^{3}He/^{4}He *Prediction, Compared with the IMAX Data*

Figure 15 shows the ^{3}He/^{4}He prediction from the propagation model using the input parameters described above and a modulation level $\phi = 750$ MV, along with the top of atmosphere ratios from IMAX. Also shown is the error band for the prediction due to the uncertainties in the input parameters. This error band was calculated by running the propagation code many times, each time varying an input parameter by a factor randomly chosen from a Gaussian distribution whose standard deviation was determined by the magnitude of the uncertainty in the input parameter. The error band shown is the quadratic sum of all the uncertainties considered.

Although the energy dependence of the IMAX data seems somewhat steeper than that of the prediction, all but one of the IMAX data points lie within the prediction error band. This indicates that the propagation history of GCR helium is indistinguishable from that of heavier GCRs, given the present uncertainties in the measurements and the model parameters.

Figure 15 also shows the prediction from the model, using the cross section for ^{3}He production from Meyer (1972) (shown in Fig. 12). If helium has the same propagation history as heavier GCRs, then the IMAX results are

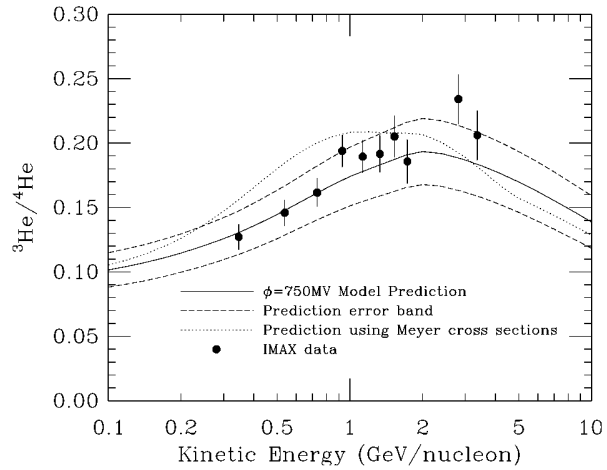

FIG. 15.—Prediction for $\phi = 750$ MV ^{3}He/^{4}He from the propagation model (*solid line*), along with the top of atmosphere ratios from IMAX. The prediction error band due to the uncertainties in the input parameters is also shown as the dashed lines. The dotted line is the prediction using the cross section for production of ^{3}He (and ^{3}H) adopted by Meyer (1972).

clearly inconsistent with a sharp peak in the cross section at ~ 1 GeV nucleon^{-1}. However, if the peak in the cross section really exists, then the IMAX results would indicate that the propagation history of helium is different from that of heavier GCRs.

Figure 16 shows the relative importance of the uncertainties in the inputs for the ^{3}He/^{4}He prediction. Clearly, the most important uncertainties are due to the mean of the path length distribution λ_e and the cross section for ^{3}He production from ^{4}He. The uncertainties due to the mass-changing cross sections, the scaling of cross sections to the helium target, and solar modulation are much less important.

A significant reduction in the uncertainty in λ_e would require an effort by the various research groups to compare their input parameters and the predictions of their leaky box propagation calculations for the B/C ratio. This would result in a better understanding of the reasons for the differences between the predictions, and hopefully a reduction in those differences would follow.

We note that complete elimination of the uncertainty in λ_e would decrease the width of the error band for our ^{3}He/^{4}He prediction by $\sim 30\%$. The uncertainties in the cross section for production of ^{3}He (and ^{3}H) can only be reduced by more experimental measurements. This is especially true above ~ 700 MeV nucleon^{-1}, where calculations based on nucleon-nucleon cross section measurements indicate the cross section should be rising, while the sparse experimental measurements indicate a flat cross section.

5.6. *Comparisons with Previous Data*

Our propagation model can also generate ^{3}He/^{4}He predictions for modulation levels appropriate for comparison with other ^{3}He/^{4}He measurements. Figure 17 shows data from the MASS and SMILI-1 balloon flights (Webber et al. 1991 and Beatty et al. 1993, respectively). The modulation levels appropriate for these data are ~ 1400 MV for MASS and ~ 1200 MV for SMILI-1. The predictions from our model for these modulation levels are in excellent agreement with these data, as indicated in the figure, again indicating consistency between the propagation histories of cosmic-ray helium and heavier GCRs. Finally, the helium isotope ratios measured by IMAX are shown in the context of previous results of ^{3}He/^{4}He measurements from the literature. Here we refrain from including a prediction from a single standard propagation model because of the variety of the specific conditions for all these measurements with respect to the solar modulation level. The predictions included in Figure 18 represent four different solar modulation levels of $\phi = 500$, 750, 1100, and 1500 MV from top to bottom. For clarity we did not include any of the uncertainties indicated in Figures 15 and 16 here. There is a tendency for previous measurements to be below the model from ~ 570 to 1200 MeV nucleon^{-1} (see also Fig. 17). The IMAX data do not show this trend (see Fig. 15). However,

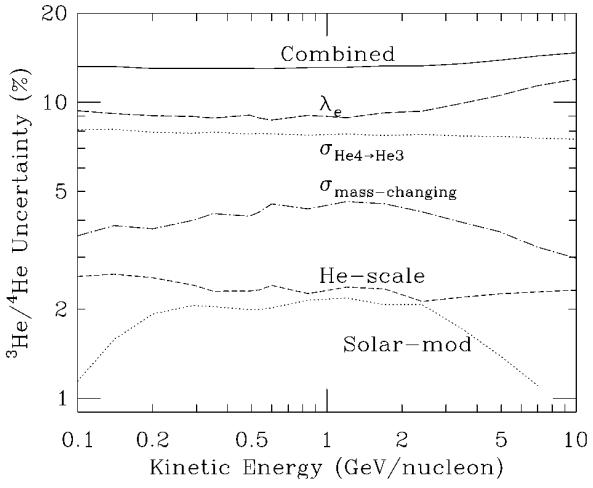

FIG. 16.—Relative contributions of the uncertainties in the important input parameters to the uncertainty in the ^{3}He/^{4}He prediction. λ_e: escape mean free path; $\sigma_{^4He\to^3He}$: cross section for ^{3}He production from ^{4}He; $\sigma_{mass\text{-}changing}$: ^{3}He and ^{4}He mass-changing cross sections; He scale: scaling cross sections to helium target; Solar-mod: solar modulation level.

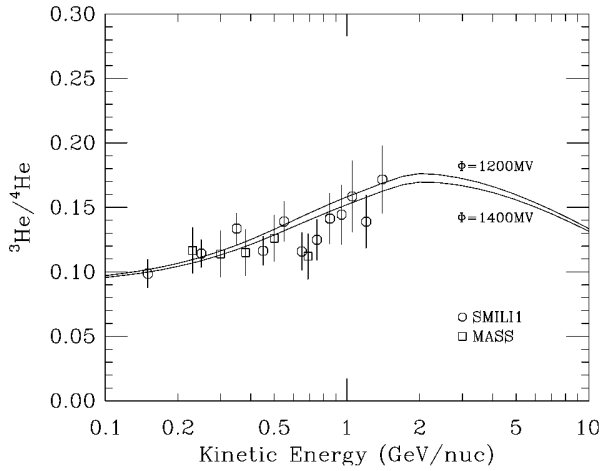

FIG. 17.—SMILI-1 and MASS ^{3}He/^{4}He measurements compared with predictions from our propagation model for modulation levels of 1200 and 1400 MV.

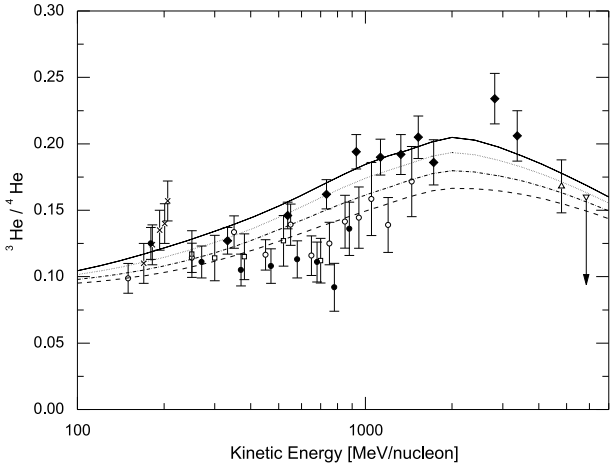

FIG. 18.—IMAX data and present ^{3}He/^{4}He measurements from literature. Data points are as follows: *cross*, Webber & Yushak (1983) ($\phi = 450$ MV); *downward-pointing triangle*, Webber et al. (1987) ($\phi = 400$ MV); *open squares*, Webber et al. (1991) ($\phi = 1.4$ GV); *open circle*, Beatty et al. (1993) ($\phi = 1.2$ GV); *filled circles*, Wefel et al. (1995) ($\phi = 1.5$ GV); *upward-pointing triangle*, Hatano et al. (1995); *filled diamonds*, this work ($\phi = 750$ MV). Also shown are predictions of our propagation model using different solar modulation parameters. From the top to bottom, ϕ is 500, 750, 1100, and 1500 MV, respectively. It reflects the range of conditions for all these measurements with respect to different solar modulation levels. Some of the data may not be corrected to the top of atmosphere.

Figure 18 shows that the cosmic-ray ^{3}He/^{4}He ratio is becoming a well-measured isotopic secondary/primary ratio now and has to be considered as a characteristic feature along with the boron/carbon and subiron/iron ratios reproduced by cosmic-ray propagation models.

5.7. *Conclusions*

IMAX has measured the cosmic-ray ^{3}He/^{4}He ratio over the energy range 0.2–3.6 GeV nucleon^{-1}. Over this energy range, the propagation of cosmic-ray helium is found to be consistent with the propagation of heavier nuclei, given the present uncertainties in the input parameters. The most important uncertainties in a galactic propagation model are due to the uncertainty of path length distributions λ_e and the cross section for production of ^{3}He from ^{4}He, found in literature. Whereas the ^{3}He/^{4}He ratio is fairly insensitive to solar modulation at energies below $\sim$100 MeV nucleon^{-1}, it becomes affected at higher energies, around the intensity maximum in the isotope spectra. Although no overabundance of ^{3}He nuclei in the cosmic radiation is indicated from measurements of the ^{3}He/^{4}He ratio, the ^{2}H/^{4}He ratio measured by IMAX will provide an independent test of the consistency of the propagation of light isotopes as well as the sensitivity of solar modulation effects. Along with measurements of the antiproton/proton ratio, the positron fraction $e^+/(e^+ + e^-)$, and heavier nuclei secondary/primary ratios, it will give us a clearer view of the galactic propagation of cosmic rays.

We thank the technical crews from New Mexico State University, Goddard Space Flight Center, California Institute of Technology, and the Universität Siegen for their dedicated support. We are grateful to the National Scientific Balloon Facility for carrying out a successful flight of the IMAX payload. The IMAX project was supported in the United States by NASA under RTOP 353-87-02 (GSFC) and grants NAGW-1418 (NMSU/BBMF) and NAGW-1919 (Caltech) and in Germany by the Deutsche Forschungsgemeinschaft (DFG) and the Bundesministerium für Bildung, Wissenschaft, Forschung, und Technologie (BMBF).

REFERENCES

Abdullin, S. K., et al. 1994, Nucl. Phys. A, 569, 753
Abdurakhimov, A. K., et al. 1991, Nucl. Phys. A, 362 , 376
Ableev, V., G. et al. 1982, Soviet J. Nucl. Phys., 36, 518
Aksinenko, V. D., et al. 1980, Nucl. Phys. A, 348, 518
Auce, A., et al. 1994, Phys. Rev. C, 50, 871
Barbiellini, G., et al. 1996, A&A, 309, L15
Barrett, R. C., & Jackson, D. 1977, Nuclear Sizes and Structure (Oxford: Clarendon Press)
Barnett, R. M., et al. 1996, Phys. Rev. D, 54, 134
Barwick, S. W., et al. 1997, ApJ, 482, L191
Beatty, J. J. 1986, ApJ, 311, 425
Beatty, J. J., et al. 1993, ApJ, 413, 268
Bizard, G., et al. 1977, Nucl. Phys. A, 285, 461
Blinov, A. V., et al. 1984, Soviet J. Nucl. Phys., 39, 161
———. 1985, Soviet J. Nucl. Phys., 42, 133
DeVries, R. M., et al. 1982, Phys. Rev. C, 26, 301
Dubar, L. V., et al. 1989, Soviet J. Nuclear Physics, 49, 771
DuVernois, M. A., Simpson, J. A., & Thayer, M. R. 1995, Proc. 24th Internat. Cosmic-Ray Conf. (Rome), 2, 589
Englemann, J. J., et al. 1990, A&A, 233, 96
Ferrando, P., et al. 1988, Phys. Rev. C, 37, 1490
———. 1991, A&A, 247, 163
Fisk, L. A. 1971, J. Geophys. Res., 76, 221
Garcia-Muñoz, M., et al. 1987, ApJS, 64, 267
Gaisser, T. K., & Schaefer, R. K. 1992, ApJ, 394, 174
Glagolev, V. V., et al. 1993, Z. Phys. C, 60, 421
Golden, R. L., et al. 1973, Nucl. Instrum. Methods, 113, 349
———. 1978, Nucl. Instrum. Methods, 148, 179
———. 1979, Phys. Rev. Lett., 43, 1196
———. 1991, Nucl. Instrum. Methods A, 306, 366
Hatano, Y., et al. 1995, Phys. Rev. D, 52, 6219
Heinbach, U., & Simon, M. 1995, ApJ, 441, 209
Hirzebruch, S., E., et al. 1993, Proc. 23d Internat. Cosmic-Ray Conf. (Calgary), 2, 175
Hof, M., et al. 1994, Nucl. Instrum. Methods A, 345, 561
Jaros, J., et al. 1978, Phys. Rev. C, 18, 2273
Jordan, S. P., & Meyer, P. 1984, Phys. Rev. Lett., 53, 505
Klem, R., et al. 1977, Phys. Lett. B, 70, 155
Krombel, K. E., & Wiedenbeck, M. E. 1988, ApJ, 208, 940
Kruger, S. T., & Heymann, D. 1973, Phys. Rev. C, 7, 2179
Labrador, A. W. 1996, Ph.D. thesis, California Inst. Tech.
Labrador, A. W., et al. 1993, Proc. 23d Internat. Cosmic-Ray Conf. (Calgary), 2, 524
Lebowitz, E., & Miller, J. M. 1969, Phys. Rev., 177, 1548
Leske, R. A. 1993, ApJ, 405, 567
Letaw, J. R., Silberberg, R., & Tsao, C. H. 1983, ApJS, 51, 271
Lloyd Owen, D., et al. 1986, Nucl. Phys. B, 274, 685
Meneguzzi, M., Audouze, J., & Reeves, H. 1971, A&A, 15, 337
Mewaldt, R. A. 1986, ApJ, 311, 979
———. 1994, Adv. Space Res., 14(10), 737
Meyer, J. P. 1972, A&AS, 7, 417
Mitchell, J. W., et al. 1993a, Proc. 23d Internat. Cosmic-Ray Conf. (Calgary), 1, 519
———. 1993b, Proc. 23d Internat. Cosmic-Ray Conf. (Calgary), 2, 627
———. 1996, Phys. Rev. Lett., 76, 3057
Nicholls, J. E., et al. 1972, Nucl. Phys. A, 181, 329
Olsen, D. L., et al. 1983, Phys. Rev. C, 28, 1602
Protheroe, R. J., et al. 1981, ApJ, 247, 362
Reimer, O. 1995, Ph.D. thesis, Universität Siegen
Sihver, L., et al. 1993, Phys. Rev. C, 47, 1225
Soutoul, A., Ferrando, P., & Webber, W. R. 1990, Proc. 21st Internat. Cosmic-Ray Conf. (Adelaide), 3, 337
Tanihata, I., et al. 1985, Phys. Lett. 160B, 380
Velichko, G. N., et al. 1985, Soviet J. Nucl. Phys., 42, 837
Webber, W. R. 1990, in AIP Conf. Proc. 203, Particle Astrophysics: The NASA Cosmic Ray Program for the 1990s and Beyond, ed. W. V. Jones, F. J. Kerr, & J. F. Ormes (New York: AIP), 294
Webber, W. R., Golden, R. L., & Mewaldt, R. A. 1987, ApJ, 312, 178
Webber, W. R., & Yushak, S. M. 1983, ApJ, 275, 391
Webber, W. R., Kish, J. C., & Schrier, D. A. 1990a, Phys. Rev. C, 41, 520
———. 1990b, Phys. Rev. C, 41, 533
———. 1990c, Phys. Rev. C, 41, 547
———. 1990d, Phys. Rev. C, 41, 566
———. 1991, ApJ, 380, 230
———. 1996, ApJ, 457, 435
Wefel, J. P., et al. 1995, Proc. 24th Internat. Cosmic-Ray Conf. (Rome), 2, 630
Yoshimura, K., et al. 1995, Phys. Rev. Lett., 75, 3792